Engineering and Computational Mechanics
Volume 168 Issue EM4

Modelling rotational failure in confined geometries using DLO
Smith and Gilbert

ice | proceedings

Proceedings of the Institution of Civil Engineers
Engineering and Computational Mechanics 168 December 2015 Issue EM4
Pages 155–168 http://dx.doi.org/10.1680/jencm.15.00016
Paper 1500016
Received 09/07/2015 Accepted 22/09/2015
Keywords: bearing capacity/limit state analysis & design/ numerical modelling

ice Institution of Civil Engineers
publishing

Modelling rotational failure in confined geometries using DLO

Colin C. Smith MA, PhD
Senior Lecturer, Department of Civil and Structural Engineering, University of Sheffield, Sheffield, UK

Matthew Gilbert BEng, PhD, CEng, MICE MASCE
Professor, Department of Civil and Structural Engineering, University of Sheffield, Sheffield, UK

Discontinuity layout optimisation (DLO) is a generally applicable numerical limit analysis procedure that can be used to identify critical plastic collapse mechanisms in engineering problems. Considering the modelling of in-plane failure, the authors have previously presented a formulation capable of identifying rotational failure mechanisms in non-dilating media. However, the formulation presented did not explicitly address cases involving confined geometries, where curved slip lines could potentially intersect boundaries. In this paper, methods are outlined which permit efficient modelling of such cases. Details of the kinematic and equilibrium formulations are provided, which are then verified through application to various geotechnical and structural mechanics problems. It is shown that results of high accuracy can be obtained, both in terms of the predicted collapse load and the corresponding failure mechanism.

Notation

$\mathbf{B}$	compatibility matrix
B	foundation width
c	cohesion
D	moment of segment between the arc and the chord
$\boldsymbol{d}$	displacements
E	energy dissipated
F	factor of safety
$\boldsymbol{f}_{\mathrm{D}}$	dead load
$\boldsymbol{f}_{\mathrm{L}}$	live load
g	acceleration due to gravity
$\boldsymbol{g}$	work coefficients
H	clay layer thickness, slope height
l	length of discontinuity
M	moment
m	number of discontinuities
$\mathbf{N}$	flow rule matrix
N_{s}	stability number
n	number of nodes, depth to stiff ground as a fraction of slope height
$\boldsymbol{p}$	plastic multipliers
$\bar{p}$	x-coordinate of centroid of the material above a specified line
$\boldsymbol{q}$	discontinuity forces/moments
S	shear force
s	relative slip across discontinuity (anti-clockwise positive)
t	nodal force variable
v	violation
W	weight of the material above a specified line
α	$\cos\theta$
β	$\sin\theta$, slope angle
λ	adequacy factor
ψ	angle subtended by an arc at its centre
ρ	density
θ	angle of discontinuity measured anti-clockwise from horizontal about a master node
ω	relative rotation

1. Introduction

Discontinuity layout optimisation (DLO) is a computational limit analysis procedure that can be used to obtain accurate upper-bound solutions for a wide range of plastic collapse problems. It differs from other established numerical methods, such as finite-element limit analysis (e.g. Lysmer, 1970; Makrodimopoulos and Martin, 2006; Sloan, 1988) and the method of characteristics (Sokolovskii, 1965), through its ability to identify directly critical failure mechanisms in the form of velocity discontinuities for a prescribed numerical discretisation, and to handle singularities in a natural and fully general way. The application of DLO to three-dimensional problem and plane-strain problems involving purely translational failure mechanisms has been described by Hawksbee *et al.* (2013) and Smith and Gilbert (2007), respectively, and to plane-strain rotational mechanisms in non-dilational materials by Smith and Gilbert (2013). Recently, a formulation suitable for the analysis of slabs has been also presented (Gilbert *et al.*,

2014). A simple exemplar MATLAB code for plane-strain translational DLO can be found in Gilbert *et al*. (2010).

Stages in the plane-strain translational DLO procedure are illustrated diagrammatically in Figures 1(a)–1(d). The limit analysis problem is couched in terms of (potential) discontinuities interlinking nodes used to discretise the solid region being modelled. Compatibility of displacements associated with discontinuities meeting at a given node is explicitly enforced, while compatibility at locations where discontinuities crossover one another away from a node is implicitly enforced. The critical layout of discontinuities is then identified using rigorous mathematical optimisation techniques (hence the name 'discontinuity layout optimisation'), with the objective being to find the solution which minimises overall energy dissipation.

Smith and Gilbert (2013) showed that curved discontinuities could alternatively be employed, as shown in Figures 1(e)–1(f), which replaces stages in Figures 1(c)–1(d). This allows fully rotational mechanisms to be modelled with high accuracy. However, as presented, the formulation only allowed unrestricted curved discontinuities to be modelled. This is a problem since in the case of confined geometries the curved discontinuities may extend beyond the domain under consideration.

In this paper, the basic DLO formulation, as previously applied to rotational problems, will initially be briefly described. Means by which rotational problems can be solved for problems involving confined geometries will then be explored, considering both primal kinematic and dual equilibrium formulations, and will cover

- modification of the yield surface for a discontinuity by accounting for the proximity of a boundary
- kinematic and equilibrium interpretation
- interpretation of equilibrium variables in relation to the operational arc shape.

Finally, the adaptive DLO procedure developed will be used to investigate a footing founded on a two-layer clay, a notched beam and two undrained slope stability problems, serving to illustrate the efficacy of the approach.

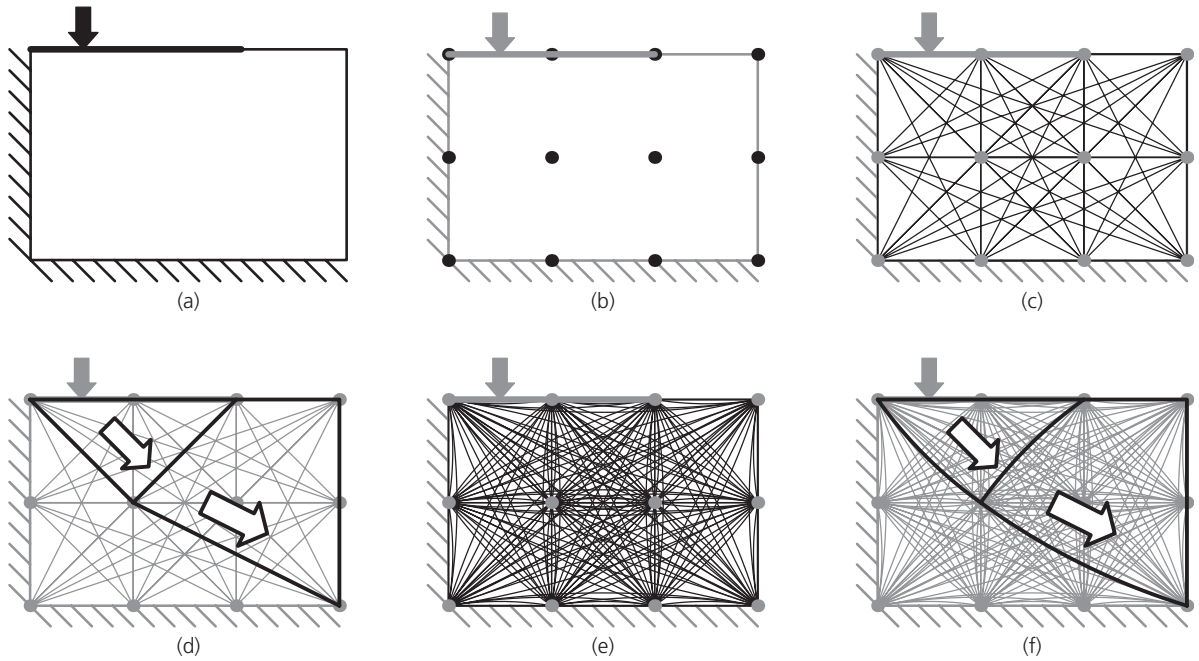

Figure 1. Stages in the DLO procedure [(a–d) translational failure; (a–b) & (e–f) rotational failure (after Smith and Gilbert, 2013)]: (a) initial problem (eccentric rigid load applied to a block of soil close to a vertical cut); (b) discretisation of soil using nodes; (c) interconnection of nodes with potential straight-line discontinuities interlinking all nodes; (d) identification of critical subset of potential discontinuities using optimisation (giving layout of slip lines in the critical translational failure mechanism); (e) interconnection of nodes with potential linear and curved discontinuities (for clarity only a small subset of possible curved discontinuities are shown); and (f) identification of critical subset of potential discontinuities using optimisation (giving the layout of slip-lines in the critical rotational failure mechanism) (after Smith and Gilbert, 2013)

2. Modelling rotational failure in DLO

2.1 General procedure

As indicated in Figures 1(a)–1(f), when using DLO a grid of nodes is first distributed across the solid region under consideration, and these nodes are then interconnected with potential straight line or curved discontinuities. Thus, when a sufficiently fine grid of nodes is employed, the set of potential discontinuities will comprise lines of a wide variety of lengths and orientations. The problem is then to find the critical collapse mechanism that satisfies compatibility and dissipates minimum energy, formed using a subset of these potential discontinuities. It can be observed that however dense the grid of nodes is, if only straight line discontinuities are employed, it is not possible to capture, for example, the failure mechanism for an eccentrically loaded footing. The solution will be the same as that for a centrally loaded footing. The use of curved slip lines in the entire domain is therefore necessary in order to capture fully all possible forms of failure mechanism.

In this paper, the focus is on Tresca materials in which rotational failure occurs along the arcs of circles. However, the principles outlined here are equally applicable to dilational Mohr–Coulomb materials where the failure lines form log spirals.

2.2 Primal energy formulation

A plane-strain analysis of a quasi-statically loaded, perfectly plastic cohesive body discretised using m nodal connections (slip-line discontinuities), n nodes and a single load case can be stated in standard matrix–vector form as follows

$$\text{1a.} \quad \min \ \lambda \boldsymbol{f}_{\mathrm{L}}^{\mathrm{T}}\boldsymbol{d} = -\boldsymbol{f}_{\mathrm{D}}^{\mathrm{T}}\boldsymbol{d} + \boldsymbol{g}^{\mathrm{T}}\boldsymbol{p}$$

subject to

$$\text{1b.} \quad \mathbf{B}\boldsymbol{d} = \mathbf{0}$$

$$\text{1c.} \quad \mathbf{N}\boldsymbol{p} - \boldsymbol{d} = \mathbf{0}$$

$$\text{1d.} \quad \boldsymbol{f}_{\mathrm{L}}^{\mathrm{T}}\boldsymbol{d} = 1$$

$$\text{1e.} \quad \boldsymbol{p} \geq \mathbf{0}$$

where the objective is to minimise energy dissipation (1a), subject to constraints enforcing energy balance (1a), nodal compatibility (1b), plastic flow (1c) and unit external work by unfactored live loads (1d). The normalisation constraint imposed by Equation 1d is required to avoid obtaining a solution in which all displacement jumps $\boldsymbol{d}$ (and thus plastic multipliers $\boldsymbol{p}$) are trivially zero or unbounded. The positivity of internal energy dissipation is ensured by inequality (1e).

Following Smith and Gilbert (2013), the full rotational compatibility relationship in (1b) for any node pair AB for geometrically unrestricted problems can be stated as follows

$$\text{2.} \quad \mathbf{B}_i\boldsymbol{d}_i = \begin{bmatrix} \alpha_i & 0{\cdot}5l_i\beta_i \\ \beta_i & -0{\cdot}5l_i\alpha_i \\ 0 & 1 \\ -\alpha_i & 0{\cdot}5l_i\beta_i \\ -\beta_i & -0{\cdot}5l_i\alpha_i \\ 0 & -1 \end{bmatrix} \begin{bmatrix} s_i \\ \omega_i \end{bmatrix}$$

where the first three lines correspond to compatibility around node A and the last three lines to compatibility around node B; α_i and β_i are, respectively, x-axis and y-axis direction cosines for slip line i, connecting nodes A and B in the direction A to B, and where s_i is the relative linear displacement across the discontinuity; l_i is the straight line length between nodes; and ω_i is the relative rotation across the discontinuity as shown in Figure 2 and according to the sign convention given in Figure 3. Summing these equations for all discontinuities connected to any node ensures translational and rotational compatibility about that node.

Such a set of equations is equivalent to starting at a point in the body adjacent to the node and traversing around the node, crossing slip lines separating one body from another, before returning to the original starting point. As slip lines are crossed, relative translational displacements and rotations accumulate; however, they must all sum to zero when the original starting point is reached.

A combination of s and ω corresponds to an arc subtended by an angle ψ, where $\omega = 2s \tan(\psi/2)/l$. Note that, in principle, $-2\pi < \psi < 2\pi$. However for any arc angle ψ, there is a kinematically equivalent angle $2\pi + \psi$ (for $\psi < 0$) or $-2\pi + \psi$ (for $\psi > 0$); this is discussed in more detail later. The small magnitude arc angles will, however, always involve less energy dissipation, and hence in practice $-\pi \leq \psi \leq \pi$.

The work equation in (1a) may be divided into two parts, the self-weight terms and the dissipation terms. The general dead load work component may be written as follows (note this is

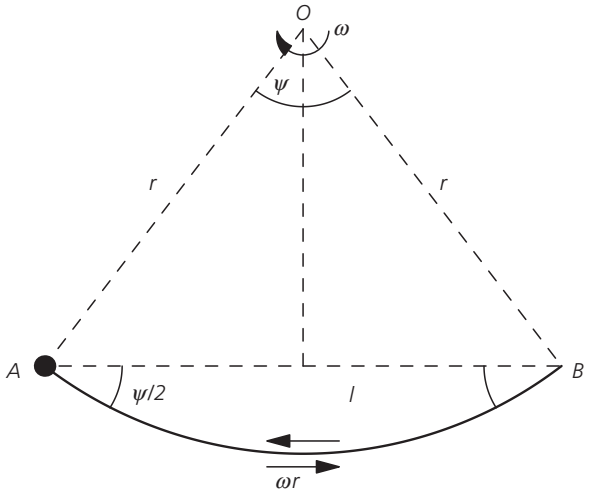

Figure 2. Slip-line geometry. The relative slip ωr across the slip line can be divided into two components parallel and normal to the nodal connection chord *AB*. At nodes *A* and *B* these resolve to the parallel component $s = \omega l/(2 \tan(\psi/2))$ and the perpendicular component $\pm 0{\cdot}5l\omega$

in a slightly different form to that presented in Smith and Gilbert, 2013)

$$3. \quad \boldsymbol{f}_{\mathrm{D}i}^{\mathrm{T}}\boldsymbol{d}_i = [-W_i\beta_i \quad -W_i\bar{p}_i - D_i]\begin{bmatrix} s_i \\ \omega_i \end{bmatrix}$$

where W_i is the total weight of the strip of the material lying vertically above chord i; $\bar{p}_i$ is the x-coordinate of the centroid of the strip of the material relative to the centre of the chord; and D_i is the moment of the segment between the arc and the chord and is constant for any arc angle

$$4. \quad D_i = \rho g \frac{l_i^3}{12}\beta_i$$

where ρ is the density of the material and g the acceleration due to gravity.

Live loads are defined similarly. Calculation of energy dissipation requires the derivation of plastic multipliers using a flow rule equation (note that ψ_i can be positive or negative)

$$5. \quad \mathbf{N}_i\boldsymbol{p}_i - \boldsymbol{d}_i = \begin{bmatrix} \dfrac{\sin\psi_i}{\psi_i} & -\dfrac{\sin\psi_i}{\psi_i} \\ \dfrac{4\ \sin^2(\psi_i/2)}{\psi_i l_i} & -\dfrac{4\ \sin^2(\psi_i/2)}{\psi l_i} \end{bmatrix} \times \begin{bmatrix} p_i^1 \\ p_i^2 \end{bmatrix} - \begin{bmatrix} s_i \\ \omega_i \end{bmatrix} = 0$$

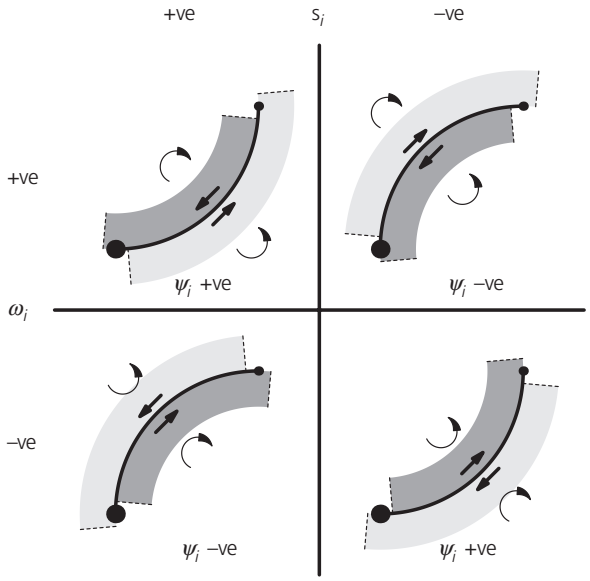

Figure 3. Sign convention for s_i and ω_i after Smith and Gilbert (2013). 'Master' node is indicated by the larger dot. ψ_i, the angle subtended by the arc at the arc centre, is positive if the arc is located on the clockwise (about the master node) side of the chord linking the nodes. s_i is positive if the relative movement vectors (straight arrows) form an anti-clockwise 'couple'. ω_i is positive if the body on the clockwise (about master node) side of the arc is moving anti-clockwise relative to the body on the other side of the arc (as indicated by curved arrows)

$$6. \quad \boldsymbol{p} \geq \mathbf{0}$$

The energy dissipation in terms of p_i is given by

$$7. \quad \mathbf{g}^{\mathrm{T}}\boldsymbol{p}$$

where $\boldsymbol{p}$ takes on the absolute value of $\boldsymbol{s}$ and where the dissipation matrix $\mathbf{g}$ is given by

$$8. \quad \mathbf{g}^{\mathrm{T}} = \{c_1 l_1, c_1 l_1, c_2 l_2, \ \ldots\ , c_m l_m\}$$

Note that Equations 5 and 8 differ slightly from the equivalent matrix in Smith and Gilbert (2013) in that all terms have been multiplied by $(\sin\psi)/\psi$. This avoids infinite terms arising across the range of possible ψ values.

2.3 Dual equilibrium form

The equivalent equilibrium formulation for a given discontinuity i is given by Smith and Gilbert (2013) as follows

$$9.\quad \mathbf{B}_i^{\mathrm{T}}\boldsymbol{t}_i + \lambda \boldsymbol{f}_{\mathrm{L}i} - \boldsymbol{q}_i = -\boldsymbol{f}_{\mathrm{D}i}$$

or in expanded form as

$$10.\quad \begin{bmatrix} \alpha_i & \beta_i & 0 & -\alpha_i & -\beta_i & 0 \\ \dfrac{l_i\beta_i}{2} & -\dfrac{l_i\alpha_i}{2} & 1 & \dfrac{l_i\beta_i}{2} & -\dfrac{l_i\alpha_i}{2} & -1 \end{bmatrix} \begin{bmatrix} t_A^x \\ t_A^y \\ t_A^m \\ t_B^x \\ t_B^y \\ t_B^m \end{bmatrix} + \lambda \begin{bmatrix} \boldsymbol{f}_{\mathrm{L}i}^{\mathrm{s}} \\ \boldsymbol{f}_{\mathrm{L}i}^{\mathrm{m}} \end{bmatrix} - \begin{bmatrix} S_i \\ M_{\mathrm{D}i} \end{bmatrix} = - \begin{bmatrix} \boldsymbol{f}_{\mathrm{D}i}^{\mathrm{s}} \\ \boldsymbol{f}_{\mathrm{D}i}^{\mathrm{m}} \end{bmatrix}$$

where $\boldsymbol{t}_i = \{t_A^x, t_A^y, t_A^m, t_B^x, t_B^y, t_B^m\}^{\mathrm{T}}$ contains nodal force variables at nodes A and B (corresponding to the nodal compatibility constraints, and where S_i and M_i, respectively, represent the shear force and moment acting on chord i ($i = 1, \ldots, m$). The required yield constraint can be written for discontinuity i as follows

$$11.\quad \mathbf{N}_i^{\mathrm{T}}\boldsymbol{q}_i \le \boldsymbol{g}_i$$

or in expanded form for the Tresca yield condition as

$$12.\quad \begin{bmatrix} \dfrac{\sin\psi_i}{\psi_i} & \dfrac{4\ \sin^2(\psi_i/2)}{\psi_i l_i} \\ -\dfrac{\sin\psi_i}{\psi_i} & -\dfrac{4\ \sin^2(\psi_i/2)}{\psi_i l_i} \end{bmatrix} \begin{bmatrix} S_i \\ M_i \end{bmatrix} \le \begin{bmatrix} c_i l_i \\ c_i l_i \end{bmatrix}$$

The shear force S and moment M are the forces/moments acting on the chord face of the solid segment delineated by the chord and arc joining the two nodes under consideration, as shown in Figure 4. Equation 12 tests whether this combination of S and M would cause yield by slip along the arc specified by ψ.

2.4 Yield surface

Equation 12 defines the yield surface for any discontinuity and may be rewritten in the form of equations relating S, M and ψ as follows (assuming $-\pi \le \psi \le \pi$)

$$13.\quad \left(\frac{S}{lc}\right)\frac{\sin\psi}{\psi} + 4\left(\frac{M}{l^2c}\right)\frac{\sin^2(\psi/2)}{\psi} \le 1$$

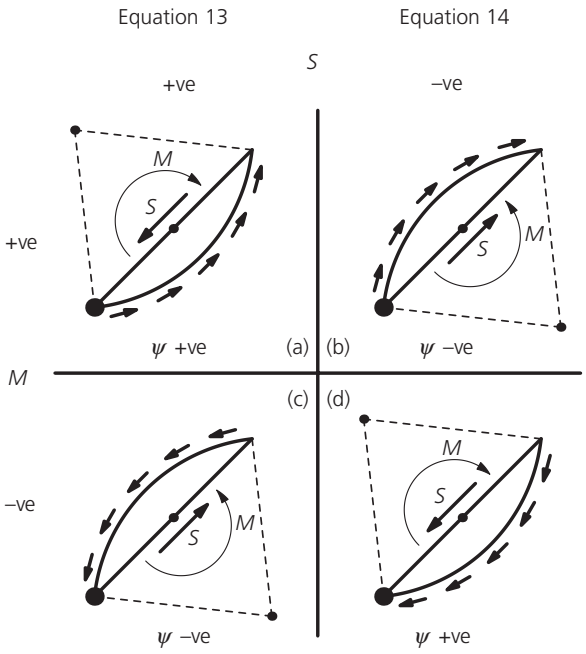

Figure 4. Interpretation and sign convention for the derived dual parameters S and M acting on the chord joining two nodes, for the different scenarios depicted in Figure 3. The sign of S is independent of the location of the master node. The sign of M is a function of the location of the master node. The small arrows on the circumference of the arc indicate the shear stresses opposing the rotation of the segment (after Smith and Gilbert, 2013)

$$14.\quad \left(\frac{S}{lc}\right)\frac{\sin\psi}{\psi} + 4\left(\frac{M}{l^2c}\right)\frac{\sin^2(\psi/2)}{\psi} \ge -1$$

The corresponding yield lines are graphically depicted in Figure 5 across the full range of arc angles ψ. These enclose the core unrestricted yield surface which has an approximately elliptical shape. Note that for the dashed lines (second constraint in Equation 12, or Equation 14), negative values of ψ apply to the upper left-hand corner of the graph.

Thus, the upper right-hand corner of the graph corresponds to Figures 3(a) and 4(a), while the upper left-hand corner of the graph corresponds to Figures 3(b) and 4(b) and so on.

It can be seen that for unrestricted boundaries, the most efficient arc (i.e. that which dissipates least energy) for pure rotation corresponds to point A which is at $S = 0$, $M = 0{\cdot}69$ and $\psi = 133{\cdot}56°$.

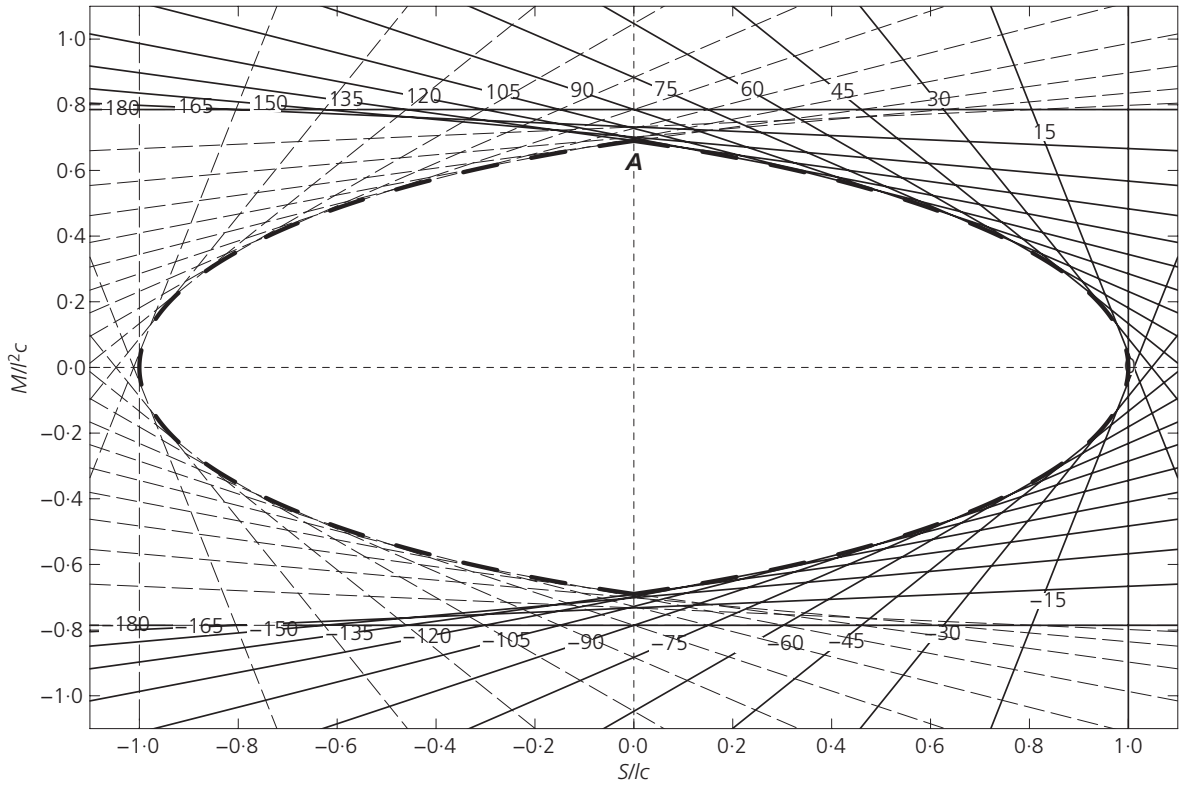

Figure 5. Yield surface in normalised shear (S)–moment (M) space (thick dashed line). Thin solid lines and dashed lines refer, respectively, to the first and second constraints in Equation 12. Numbers on lines indicate the value of ψ in degrees and are plotted on solid lines only for clarity

3. Yield surface in the presence of a boundary

3.1 Background

Consider a chord AB within a single body adjacent to a boundary of arbitrary form as depicted in Figure 6. Standard geometrical methods exist to determine the largest arc spanning AB that does not intersect the boundary. Let the limiting arc be described by subtending angle $\psi_{\min}$ for arcs on the anti-clockwise side of the chord relative to the master node and $\psi_{\max}$ for arcs on the clockwise side.

In the primal kinematic formulation, the only additional requirement is to restrict ψ such that $\psi_{\min} < \psi < \psi_{\max}$ (where negative ψ lies on the anti-clockwise side of the line).

In the dual equilibrium formulation, the presence of the boundary increases the size of the yield surface for the relevant chord. An example is given in Figure 7 for $\psi_{\max} = 45°$ with $\psi_{\min}$ unrestricted. A solution at point B shows that the same energy is dissipated for an angle $\psi = 45°$ or $\psi = -159°$. If there is a restriction on the other side of the line (i.e. there is an additional minimum value $\psi_{\min}$) then the yield surface is restricted further on the other quadrants of the yield surface.

Any point on the yield surface corresponds to a unique arc angle ψ with the exception of the distinct corners (e.g. point A in Figure 5 or B in Figure 7). At these locations, the point corresponds to a range of arc angles. For example, in the case of point B in Figure 7, the range is $45° < \psi < 180°$, $-180° < \psi < -159°$ and it is not possible to determine the exact angle from the dual solution. However, in kinematic terms, this arc is actually made of a linear combination of two arcs, one with $\psi = -159°$ and the other with $\psi = 45°$. The kinematic theory behind this is given in Section 3.2.

3.2 Kinematic combination of two slip-lines

3.2.1 Kinematic equivalence

Consider discontinuity AB with two slip-lines assigned to it, with angles ψ_1 and ψ_2, and each with a slip s_1 and s_2. Purely in terms of kinematics, the effect across the discontinuity is equivalent to a single slip line with angle ψ and slip s,

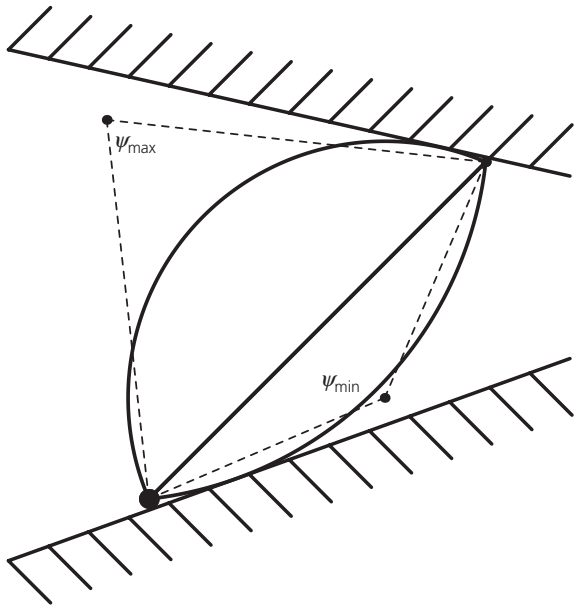

Figure 6. Slip-line arc size restricted by boundary. The main node is indicated by the larger dot

such that

15. $$s = s_1 + s_2$$

16. $$\omega = \omega_1 + \omega_2$$

or, equivalently,

17. $$s \tan(\psi/2) = s_1 \tan(\psi_1/2) + s_2 \tan(\psi_2/2)$$

Let

18. $$T^+ = \frac{\tan(\psi_1/2) + \tan(\psi_2/2)}{2}$$

19. $$T^- = \frac{\tan(\psi_1/2) - \tan(\psi_2/2)}{2}$$

Then

20. $$\tan(\psi_1/2) = T^+ + T^-$$

21. $$\tan(\psi_2/2) = T^+ - T^-$$

It can be shown that

22. $$\begin{aligned}\tan(\psi/2) &= T^+ + T^-\left(\frac{1 - s_2/s_1}{1 + s_2/s_1}\right) \\ &= T^+ + T^- \tan\left(\pi/4 - \tan^{-1}\left(\frac{s_2}{s_1}\right)\right)\end{aligned}$$

Thus, for any ratio of s_2 and s_1, it is possible to determine the equivalent angle ψ.

For ψ to lie between ψ_1 and ψ_2, it is necessary for $-1 < \tan(\pi/4 - \tan^{-1}(s_2/s_1)) < 1$, which requires $s_2/s_1 > 0$ (i.e. s_1 and s_2 must share the same sign). In terms of the dual yield surface this is equivalent to both slip-lines being either on the left-hand side or on the right-hand side of the yield surface.

3.2.2 Work done against body forces

From superposition, for n slip lines linking any single pair of nodes, the work done is given by

23. $$E = \sum_{i=1}^{n}[-W_i\beta_i\,(-W_i\bar{p}_i - D_i)]\begin{bmatrix} s_i \\ \omega_i \end{bmatrix}$$

Since W, $\bar{p}$, D are same for all slip-lines that connect the same pair of nodes, Equation 23 becomes

24. $$E = [-W\beta\,(-W\bar{p} - D_i)]\sum_{i=1}^{n}\begin{bmatrix} s_i \\ \omega_i \end{bmatrix}$$

Substituting extended versions of Equations 15 and 16

25. $$E = [-W\beta\,(-W\bar{p} - D_i)]\begin{bmatrix} s \\ \omega \end{bmatrix}$$

Hence, there is no effect on the work done against body forces by replacing multiple slip-lines linking a single pair of nodes with one kinematically equivalent slip line.

3.2.3 Energy dissipation

The energy dissipated by one equivalent slip-line is given by

26. $$E_{1L} = cl\left(\frac{\psi|s|}{\sin\psi}\right),$$

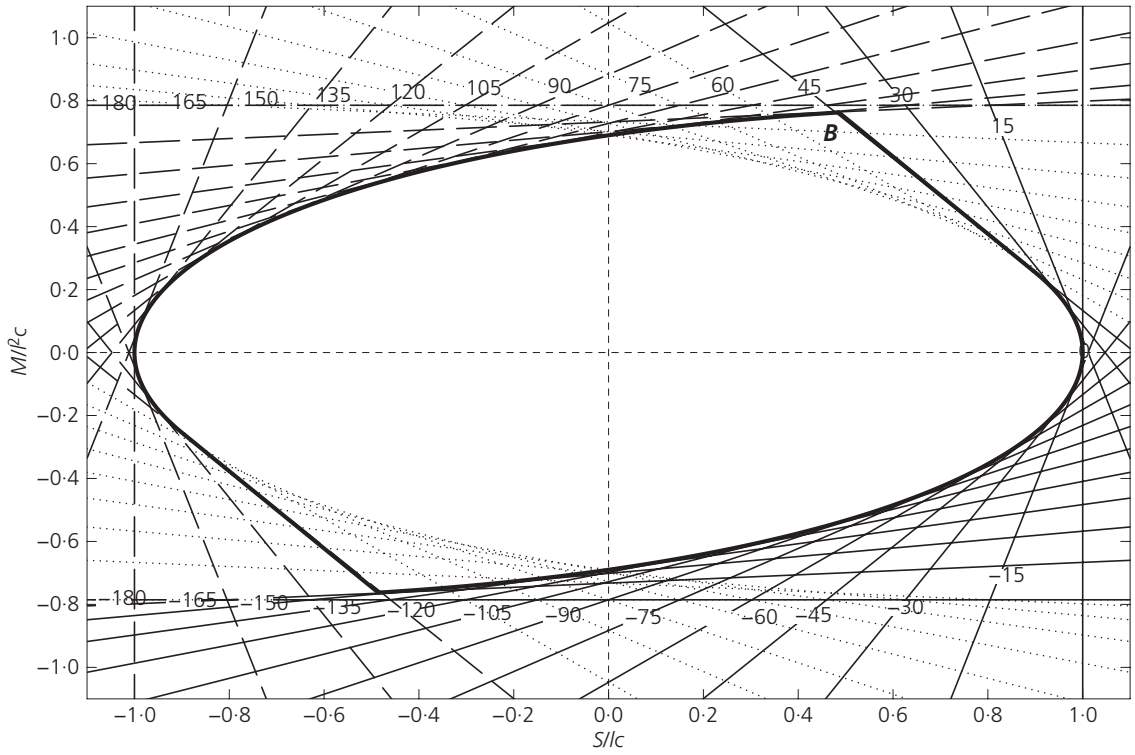

Figure 7. Yield surface in normalised shear (S)–moment (M) space (thick line), where there is a single boundary restriction $\psi_r = 45°$. Thin solid lines and dashed lines refer, respectively, to the first and second constraints in Equation 12. Numbers on lines indicate the value of ψ in degrees and are plotted on solid lines only for clarity

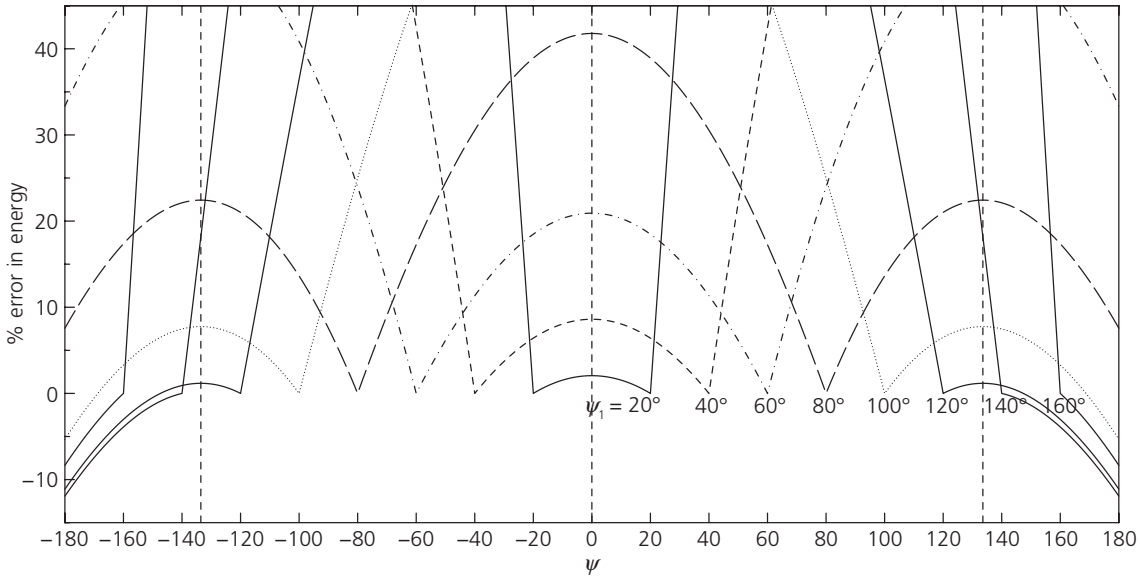

Figure 8. Percentage error in energy dissipation by linearly combining two symmetrical arcs of various subtending angles $\pm\psi_1$. Angle ψ is the combined single arc angle. The peaks in the curves occur at $\psi = -133{\cdot}56°$, 0° and 133·56°

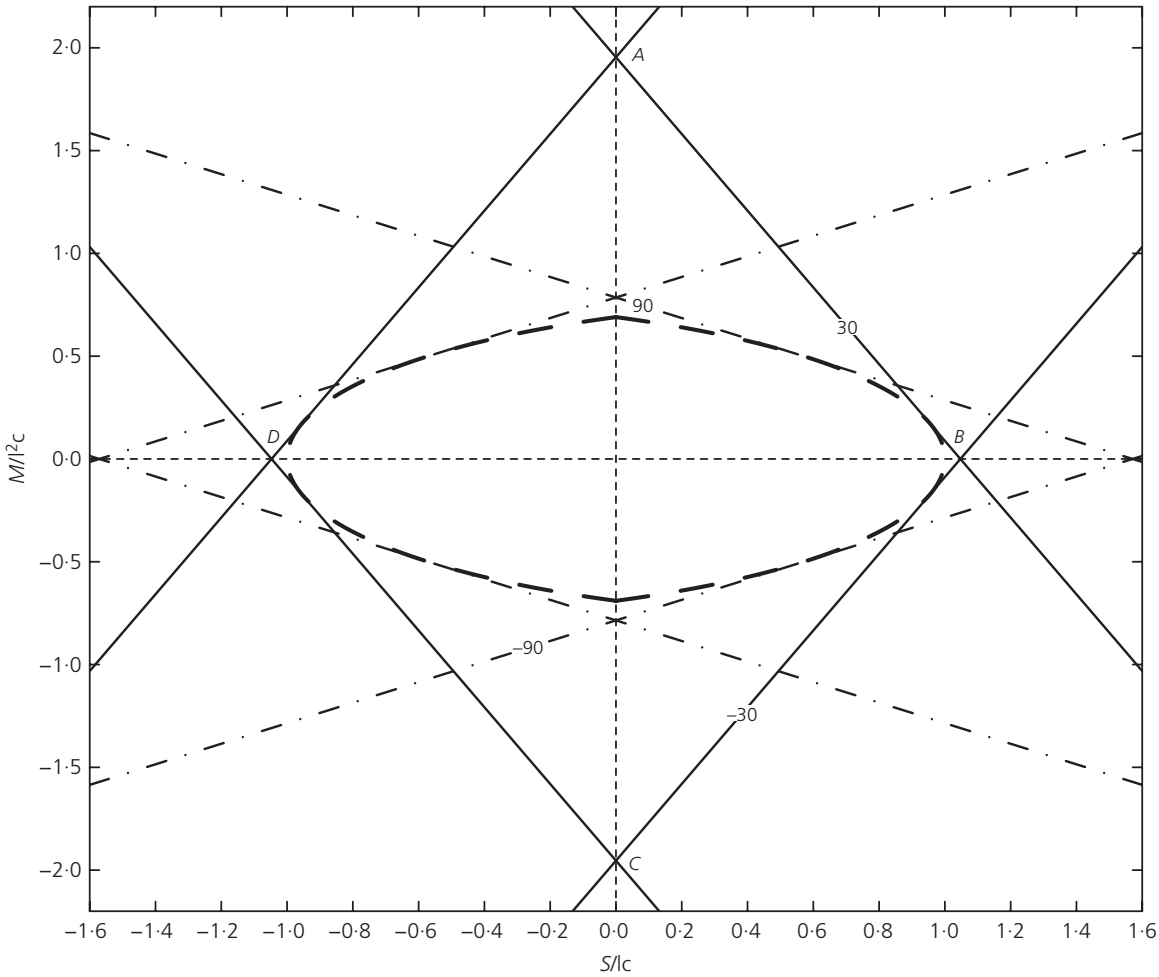

Figure 9. Yield surface, $\psi = \pm 30°$ and $\psi = \pm 90°$

and the energy dissipated by the two lines separately will be

$$E_{2L} = cl\left(\frac{\psi_1|s_1|}{\sin\ \psi_1} + \frac{\psi_2|s_2|}{\sin\ \psi_2}\right) \quad 27.$$

The error in energy dissipation associated with modelling a single arc with subtending angle ψ using two symmetrical arcs of angle $\pm\psi_1$ is shown in Figure 8. It is seen that the maximum error inside the original arcs occurs at the centre where $\psi = 0$, $s_1 = s_2$ and, using Equation 27, is equal to $100((\psi_1/\sin\ \psi_1) - 1)$. For $\psi = 30°$, the error is $\sim 4{\cdot}7\%$; for $\psi = 10°$, the error is $\sim 0{\cdot}5\%$; and for $\psi = 1°$, the error is $\sim 0{\cdot}005\%$.

It is also seen that where the equivalent arc lies outside the original arc pair, the error increases very rapidly with ψ. In the context of the dual solution, in the case where s_1 and s_2 share the same signs, then this corresponds to either point B or point D in Figure 9 and it is clear that the distance from the core yield surface is small. However, if the signs of s_1 and s_2 differ, then this corresponds to point A or point C and the distance from the standard yield surface is large.

Conversely, and as also shown in Figure 9, if the arc pairs are larger (for example, $\psi = 90°$), it can be seen that the deviation is small when the signs of s_1 and s_2 differ, and large if they are the same. This is shown in Figure 8. It can be seen that for angles of $\psi_1 > 133{\cdot}56°$, it is possible for the line pair to be more efficient than the single equivalent line. However, this will never happen in practice since for angles $\psi > 133{\cdot}56°$ there will always be an angle of the opposite sign, which corresponds to a lower energy solution (if this is not possible due to the proximity of a boundary then the symmetrical line pair in this example will also not be possible).

3.2.4 Implication for DLO solutions

When graphically displaying a DLO solution, for clarity it is simplest to depict an arc according to the values of s and ω, determined for that connection where $\psi = 2 \arctan(\omega l/s)$. However, during the adaptive phase of the solution, it is possible for an apparently illegal curved slip line to be predicted (i.e. one which crosses a boundary) due to the combination of two yield conditions, as for example shown by point B in Figure 7. In this case, the two constituent slip lines should be displayed. These can be determined from the plastic multipliers $\boldsymbol{p}$. However, in general, these will be progressively replaced with more efficient, legal, slip lines.

4. Adaptive solution procedure

4.1 Background

The solution procedure outlined in Section 2 becomes computationally expensive when large numbers of nodes are involved. Smith and Gilbert (2007, 2013) demonstrated that the solution process can be significantly accelerated by solving a simple initial starting problem, involving a reduced number of slip-line discontinuities between nodes, and then enriching this by way of adaptive addition of additional slip lines that are found to violate yield (based on the dual solution).

For simplicity, if the domain is divided into several bodies of differing material properties, then it is convenient to confine slip lines so as to lie entirely within a single body. If a critical arc does span two bodies, the solver will be able to model this in a piecewise manner, within the respective bodies (in practice the slip line is unlikely to be unchanged from one body to another).

4.2 Initial starting problem

The initial starting problem should be devised so as to permit a viable kinematic mechanism to be found using the minimum number of variables and constraints, in the interests of computational efficiency. To this end, slip-line discontinuities are only placed between nodes and their nearest neighbours. Moreover, only four constraints per slip-line discontinuity are initially used to (approximately) define the yield surface.

For an unrestricted nodal connection, the yield surface can initially be represented by four linear constraints, corresponding to $\psi = 0°$ and 180° in Equations 13 and 14, and shown in Figure 10(a). This corresponds to two straight lines and two semi-circular slip lines, allowing slip in both directions in each case. Note that if a slip line is not restricted, then using M/l^2 $c = \pm 0{\cdot}69$ is preferable as it coincides with the upper and lower edges of the yield surface, indicated by the horizontal dashed lines shown in Figure 10(a).

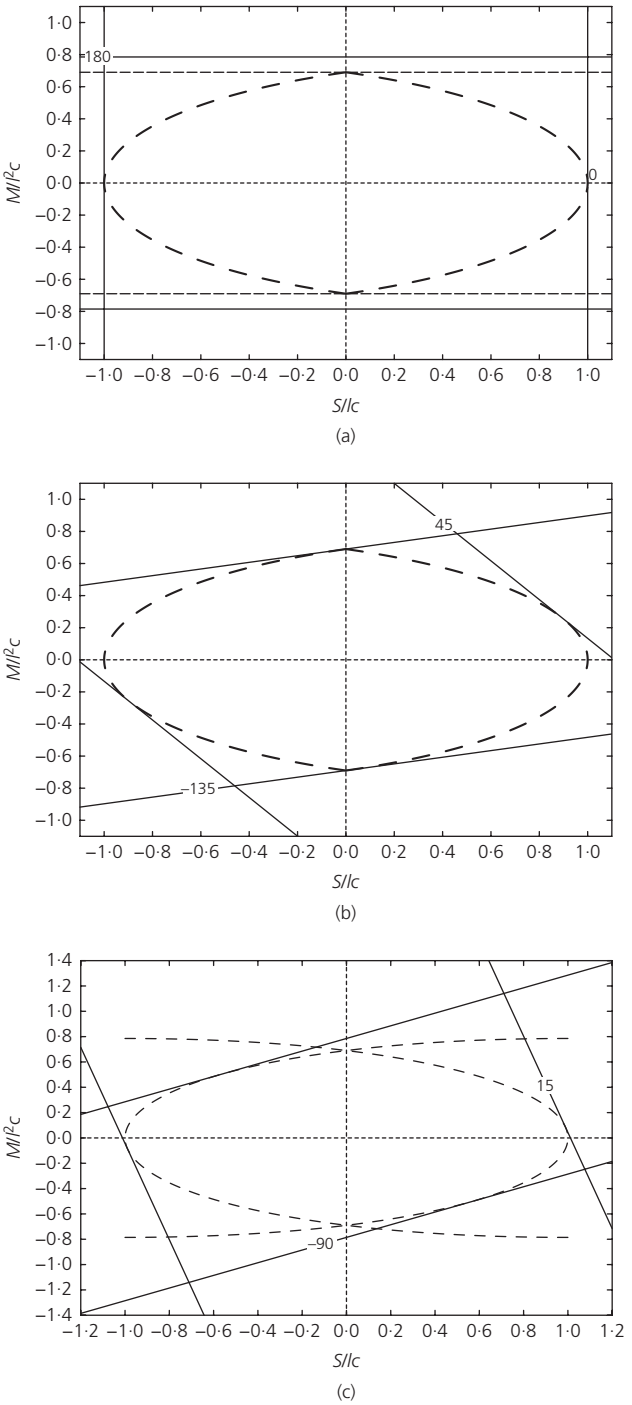

Figure 10. Proposed initial yield surfaces (indicated by solid lines) for: (a) no restrictive boundaries, (b) single restrictive boundary, $\psi_{max} = 45°$; and (c) two restrictive boundaries, $\psi_{min} = -90°$, $\psi_{max} = 15°$

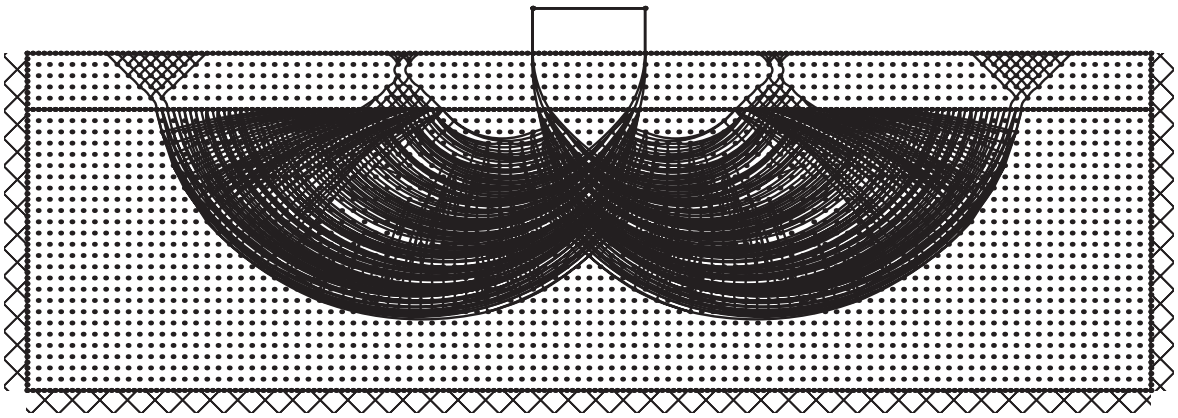

Figure 11. Failure mechanism for a two-layer clay problem, upper layer strength $c = 1$, lower layer strength $c_l = 0{\cdot}2$, footing width B, upper layer thickness H, fully rough footing, $H/B = 0{\cdot}5$, nodal spacing $B/10$. Collapse load $= 2{\cdot}31cB$

For a case involving a single restrictive boundary, corresponding to an arc angle ψ, for simplicity the other line is set to $180 + \psi$ for $\psi < 0$ and $\psi - 180$ for $\psi > 0$ to keep the overall initial yield surface relatively well represented, as shown in Figure 10(b). If both sides are restrictive, for example, $\psi = 15°$ and $-90°$, the initial yield surface is simply set using both angles, as shown in Figure 10(c).

4.3 Adaptive method

Violation of the yield surface, as determined using the dual formulation, leads to the addition of an arc that provides the (assumed) best way to eliminate violation (this also adds an additional straight line constraint to the yield surface diagram). It is important to distinguish between: (*a*) an existing slip-line discontinuity between two nodes for which an (s, ω) pair exists in the compatibility equation (1b); (*b*) a potential slip-line discontinuity between a pair of nodes, which is not yet represented in the relevant solution matrices, but for which the dual equilibrium forces can be computed; (*c*) a plastic multiplier (or equivalent dual yield constraint) which can be associated with an (s, ω) pair, by way of Equation 1c, using a specific value of ψ. Restrictions in arc angle ψ for any slip-line discontinuity may be designated by $\psi_{\min}$ and $\psi_{\max}$ and will be equal to $\mp 180°$ for unconstrained slip lines.

The proposed adaptive algorithm is as follows.

(*a*) Loop through all existing and potential slip-line discontinuities between node pairs.

(*b*) In the case of a potential slip-line discontinuity, assume $\psi_{\min} = -180°$ and $\psi_{\max} = 180°$, and check for violation of Equations 13 and 14 in the range $\psi_{\min} < \psi < \psi_{\max}$. There may be up to two violations. Store the largest violation v and the corresponding angle ψ_v (possible restrictive boundaries are not checked at this stage for computational efficiency).

(*c*) In the case of an existing slip-line discontinuity, $\psi_{\min}$ and $\psi_{\max}$ will have previously been computed and stored. Check for violation of Equations 13 and 14 in the range $\psi_{\min} < \psi < \psi_{\max}$. There may be up to two violations. Store the largest violation v and the corresponding angle ψ_v.

(*d*) Sort all violations according to the magnitude of v. Select the top n violations, where n is typically around 10% of the full set of violations.

(*e*) For the top n violations.

(i) if a potential slip-line discontinuity occurs, check for the restricting boundaries and store the corresponding $\psi_{\min}$ and $\psi_{\max}$ values. The maximum violation may change as a result and is recomputed together with a revised ψ_v. Add an (s, ω) pair into the compatibility equation. If the recomputed violation >1·0 then add the associated plastic multiplier terms using ψ_v.

(ii) if an existing slip-line discontinuity occurs, add additional plastic multiplier terms using ψ_v.

(*f*) Repeat from (*a*) until no violations remain.

The numerical value of the violation v is computed using the left-hand side of Equation 13 or 14 as appropriate. The addition of the plastic multiplier terms using ψ_v corresponds to an additional potential curved slip line in the kinematic formulation, but allowing relative displacement in only one direction.

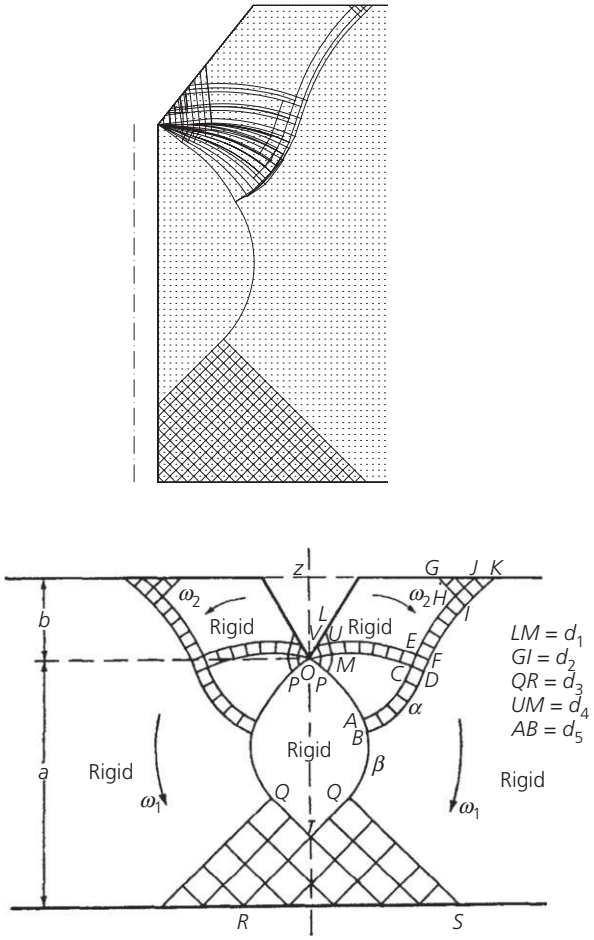

Figure 12. Failure mechanism for a shallow notched beam in pure bending (DLO solution above, $a = 0{\cdot}75$, $b = 0{\cdot}25$, notch mouth width = 0·4; Green's solution below for comparison, collapse load not given in original paper)

5. Examples

5.1 Footing on two-layer clay soil

The problem of a footing on a two-layer clay is interesting in that for a weak clay over strong clay scenario, the mechanism will be almost entirely translational, whereas for a strong clay over weak clay scenario, the mechanisms will have significant rotational elements. An example of the mechanism is given in Figure 11, with the corresponding collapse load of 2·31 ($\times cB$). This compares favourably with the solutions derived by Merifield (1999) for this problem, of 2·16 (lower bound) and 2·44 (upper bound) (average = 2·30).

5.2 Bending of a shallow notched beam

The problem of bending of a shallow notched beam was classically investigated by Green (1956), who showed that a number of different slip-line mechanism topologies could be obtained depending on the notch geometry. An example mechanism is given in Figure 12, with the corresponding DLO computed collapse bending moment per unit width $M = 0{\cdot}3519c$. The mechanism is clearly very similar in form to that postulated by Green.

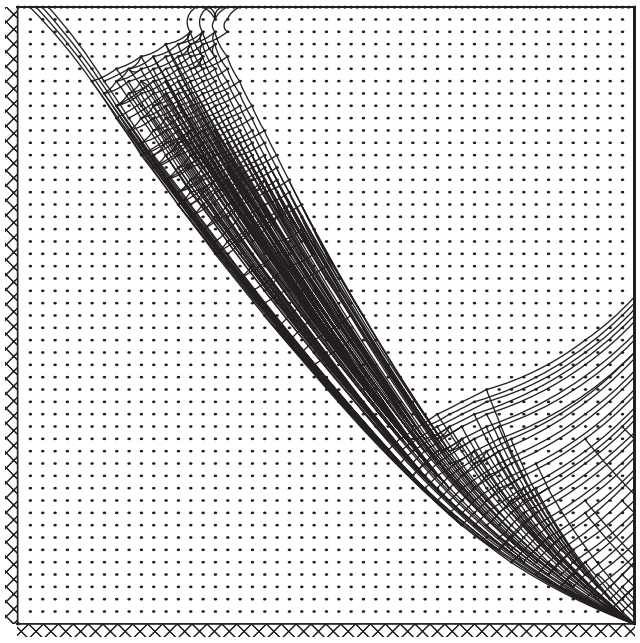

Figure 13. Vertical cut problem $\beta = 90°$, $n = 1{\cdot}0$, nodal spacing $H/50$. $N_s = 3{\cdot}783$

5.3 Undrained slope stability

This problem was classically investigated by Taylor (1937) who produced a series of stability charts based on single slip circles for a range of slope angles β, slope heights H, soil unit weights $\rho \boldsymbol{g}$ and depths to stiff ground beneath the crest of the slope of nH. Results were quoted in terms of stability number N_s which is given by

$$N_s = \frac{\rho g H F}{c} \qquad 28.$$

where F is the factor of safety on the undrained shear strength c.

For the case of a vertical cut ($\beta = 90°$), the solution given in Figure 13 is obtained with $N_s = 3{\cdot}783$. This compares well (numerically within 0·2%) with the solution by Martin (2011), who derived what may be regarded as a highly accurate solution of 3·77649 using the method of characteristics. For a shallower slope, $\beta = 20°$, $n = 1{\cdot}2$, Taylor predicts a stability

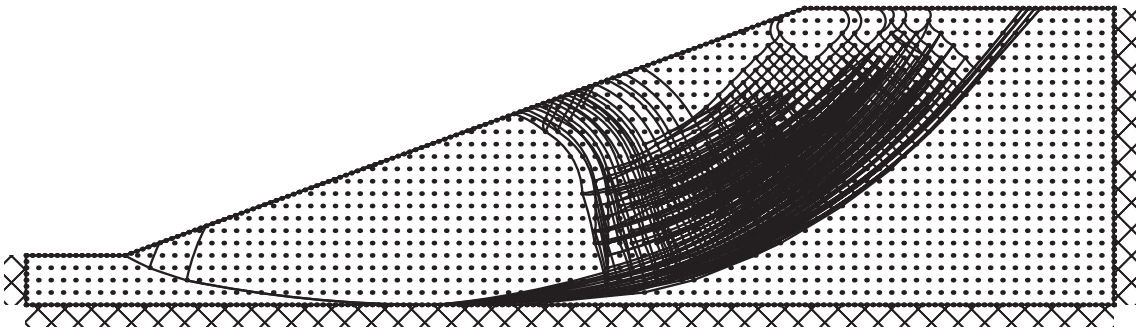

Figure 14. Undrained slope angle $\beta = 20°$, $n = 1{\cdot}2$, nodal spacing $H/20$. $N_s = 7{\cdot}905$ (compared with 7·94 from Taylor)

number $N_s = 7{\cdot}95$ and a toe mechanism. The DLO analysis also predicts a toe mechanism as shown in Figure 14, with a slightly lower value of $N_s = 7{\cdot}905$.

6. Discussion

In the algorithm presented, restrictive boundaries are checked only in the case of slip-line discontinuities, which are already represented in the solution matrix. This is efficient since typically only 1–5% of all potential slip-line discontinuities ever become represented in the solution matrix in the adaptive solution procedure. In addition, as the adaptive solution becomes closer to the final solution, adaptively added slip lines will automatically sit between any restrictive boundaries since the new slip lines are based on a solution that already implicitly accounts for the presence of these boundaries. Hence, few new slip lines will be considered that are subsequently required to be rejected for violating a restrictive boundary. For the problems presented here it was possible to get to within 1% of the best available solution in the literature in under 10 s using a PC running an Intel Core i7-2640M CPU at 2·80 GHz with 8 GB RAM on a 64 bit system. Implementation of boundary checking led to little change in solution time. However, achievement of greater accuracy does require significantly longer run times, as has been previously observed by, for example, Smith and Gilbert (2013).

As can be seen in the examples presented, the inherent ability of DLO to handle singularities remains a key advantage of the procedure. Singularities are a common feature of many solutions; for example, the two-layer clay problem in particular is made up almost entirely of intersecting sets of curved fan zones in the lower layer.

7. Conclusions

(*a*) The theory presented by Smith and Gilbert (2013) that allowed modelling of rotational failure mechanisms in cohesive media using DLO has been extended to deal with problems involving confined geometries.

(*b*) A corresponding theory has been developed, considering both the primal kinematic and dual equilibrium forms.

(*c*) Application to classical problems involving a footing on two layers of clay, a notched beam in bending and the stability of a slope has been described, demonstrating the ability of the method to find accurate upper-bound solutions for problems involving confined geometries.

(*d*) It is demonstrated that pairs of slip lines may be combined to give the same kinematic effect as a single slip line, although these will involve higher energy dissipation. Depending on the formulation of the linear programming problem, this can in rare cases lead to an apparently geometrically illegal slip line which is in fact made up of two legal slip lines; however, this is straightforward to detect.

Acknowledgements

The study described was undertaken with the support of EPSRC, under grant reference EP/I014489/1. Thanks are also due to Dr Wael Darwich, who assisted with the programming of the methods described herein.

REFERENCES

Gilbert M, Smith CC, Haslam IW and Pritchard TJ (2010) Application of discontinuity layout optimization to geotechnical limit analysis problems. In *Proceedings of the 7th European Conference on Numerical Methods in Geotechnical Engineering* (Benz T and Nordal S (eds)). Trondheim, Norway, pp. 169–174.

Gilbert M, He L, Smith CC and Le CV (2014) Automatic yield-line analysis of slabs using discontinuity layout optimization. *Proceedings of the Royal Society A* **470**: 20140071, http://dx.doi.org/doi:10.1098/rspa.2014.0071.

Green A (1956) The plastic yielding of shallow notched bars due to bending. *Journal of the Mechanics and Physics of Solids* **4(4)**: 259–268.

Hawksbee S, Smith CC and Gilbert M (2013) Application of discontinuity layout optimization to three-dimensional plasticity problems. *Proceedings of the Royal Society A* **469**: 20130009, http://dx.doi.org/doi:10.1098/rspa.2013.0009.

Lysmer J (1970) Limit analysis of plane problems in soil mechanics. *Journal of the Soil Mechanics and Foundations Division ASCE* **96(4)**: 1311–1334.

Makrodimopoulos A and Martin C (2006) Lower bound limit analysis of cohesive-frictional materials using second-order cone programming. *International Journal for Numerical Methods in Engineering* **66(4)**: 604–634.

Martin C (2011) The use of adaptive finite-element limit analysis to reveal slip-line fields. *Geotechnique Letters* **1(2)**: 23–29, http://dx.doi.org/10.1680/geolett.11.00018.

Merifield RS (1999) Rigorous plasticity solutions for the bearing capacity of two-layered clays. *Géotechnique* **49(19)**: 471–490, http://dx.doi.org/10.1680/geot.1999.49.4.471.

Sloan SW (1988) Lower bound limit analysis using finite elements and linear programming. *International Journal for Numerical and Analytical Methods in Geomechanics* **12(1)**: 61–77.

Smith C and Gilbert M (2007) Application of discontinuity layout optimization to plane plasticity problems. *Proceedings of the Royal Society A* **463**: 2461–2484, http://dx.doi.org/doi:10.1098/rspa.2006.1788.

Smith CC and Gilbert M (2013) Identification of rotational failure mechanisms in cohesive media using discontinuity layout optimisation. *Geotechnique* **63(14)**: 1194–1208, http://dx.doi.org/doi:10.1680/geot.12.P.082.

Sokolovskii V (1965) *Statics of Granular Media*. Pergamon Press, Oxford, UK.

Taylor DW (1937) Stability of earth slopes. *Journal of the Boston Society of Civil Engineers* **XXIV(3)**: 337–386.